

Assessment of averaged 1D models for column adsorption with 3D computational experiments

M. Agualeles & F. Font

February 10, 2025

Abstract

In the present manuscript, we formulate a 3D mathematical model describing the capture of a contaminant in an adsorption column. The novelty of our approach involves the description of mass transfer by adsorption via an evolution equation defined on the surface of the porous media, while Stokes flow and an advection-diffusion equation describe the contaminant transport through the interstices. Numerical simulations of the 3D model on different porous geometries, with the same porosity but different microstructure, have revealed a minimal impact of the microstructure on contaminant distribution within the column. Of particular interest is the little variation in the radial direction. Then, assuming a fine structure made of a periodic array of spheres and employing homogenization theory, we have rigorously derived an averaged 1D model of column adsorption. The model has the same mathematical form than the standard 1D column adsorption model, but contains a dispersion coefficient that explicitly incorporates microstructural details of the porous media. Consequently, our model offers a theoretical foundation for the widely used 1D model in the literature. Lastly, we compare the numerical solution of the 1D model with numerical simulations of the 3D model. The concentration profiles of the 1D model closely match the cross-section averaged concentration profiles of the 3D model. Likewise, the contaminant breakthrough curves at the outlet of both models are nearly indistinguishable. These results confirm the reliability of 1D models for investigating, optimizing, and aiding in the design of column adsorption processes for practical applications.

1 Introduction

Adsorption columns play a crucial role in mitigating environmental pollutants, including greenhouse gases, volatile organic compounds and emerging contaminants [1, 2, 3]. Column sorption involves directing a fluid through a tube packed with an adsorbent material that can selectively capture specific components from the fluid through chemical or physical interactions [4] (see illustration in Fig. 1). They are widely used in various applications such as water treatment, biogas purification, and the production of biopharmaceuticals [5, 6, 7]. These systems are relatively simple to integrate into industrial processes and can be applied to both liquid and gas-phase contaminants, making them an essential technology for environmental remediation. Despite the environmental benefits, the higher costs associated with current capture

technologies diminish their economic appeal. Mathematical models can help address this challenge by providing insights into adsorption kinetics, mass transfer dynamics and column design parameters, enabling more efficient system optimization.

Existing mathematical models for adsorption often focus on highly idealized scenarios and many widely accepted solutions often deviate from the model's foundational assumptions, exhibit unrealistic parameter dependencies, and yield predictions that can be significantly inaccurate (see for instance [8]). Recently, several publications have made substantial progress in rigorously establishing robust mathematical models based on the physio-chemistry of adsorption processes (see [9, 10, 11, 12, 13, 14], among others). One important contribution in most of these works is the derivation of approximate analytical expressions for the breakthrough curve, i.e. the evolution of the mean concentration at the outlet. Deriving these analytical expressions requires formulating and solving a 1D model for the cross-sectional average concentration and adsorbed fraction of the contaminant, $c(x, t)$ and $q(x, t)$, in the column. These expressions are particularly useful for inferring system parameters by fitting them to experimental data.

For incompressible flows with low contaminant concentrations where mass loss due to adsorption may be neglected the one-dimensional model for column adsorption is found to be:

$$\frac{\partial c}{\partial t} + u \frac{\partial c}{\partial x} = D \frac{\partial^2 c}{\partial x^2} - \frac{\rho_b}{\phi} \frac{\partial q}{\partial t}, \quad x \in (0, L), t \in (0, \infty), \quad (1a)$$

$$\frac{\partial q}{\partial t} = k_{\text{ad}} c^m (q_{\text{max}} - q)^n - k_{\text{de}} q^n, \quad x \in (0, L), t \in (0, \infty), \quad (1b)$$

$$c(x, 0) = q(x, 0) = 0, \quad x \in (0, L), \quad (1c)$$

$$uc_{\text{in}} = \left(uc - D \frac{\partial c}{\partial x} \right)_{x=0^+}, \quad \left. \frac{\partial c}{\partial x} \right|_{x=L^-} = 0, \quad t > 0. \quad (1d)$$

where u is the interstitial velocity, D is the dispersion coefficient, ρ_b is the density of the bulk material (defined as the ratio of the mass of adsorbent to the column volume), m, n are the global orders of the adsorption reaction, $k_{\text{ad}}, k_{\text{de}}$ are the adsorption and desorption rates and q_{max} is the maximum adsorbed fraction that the adsorbent material can achieve. See [12] for details on a derivation of system (1). Note that D accounts for molecular diffusion as well as axial dispersion caused by microstructural obstacles encountered by contaminant molecules along their path. Theoretical prediction of dispersion effects due to the porous media microstructure is generally complex. Homogenization theory can be used to obtain theoretical estimates of dispersion coefficients [15], though its application is limited to relatively simple porous media structures. In column adsorption models, the value of D is typically determined through experimental correlations [16, 17].

This work is the first in a series aimed at systematically investigating the impact of the adsorbent's structure on filter performance, with a particular focus on assessing its influence on breakthrough curves. We begin by formulating a system of partial differential equations for the contaminant concentration in the fluid region of a general 3D filter configuration, explicitly determining the boundary conditions at the surfaces where the adsorption reaction occurs. Surface reactions are inherently complex and involve several phenomenological parameters, such as adsorption and desorption rates, whose direct measurement is virtually impossible. Existing column adsorption models provide expressions for these reactions that are valid only from an averaged perspective, incorporating them as a lumped sink term in the governing equation for contaminant transport (see, for instance, [18, 19]). Thus, our first contribution is

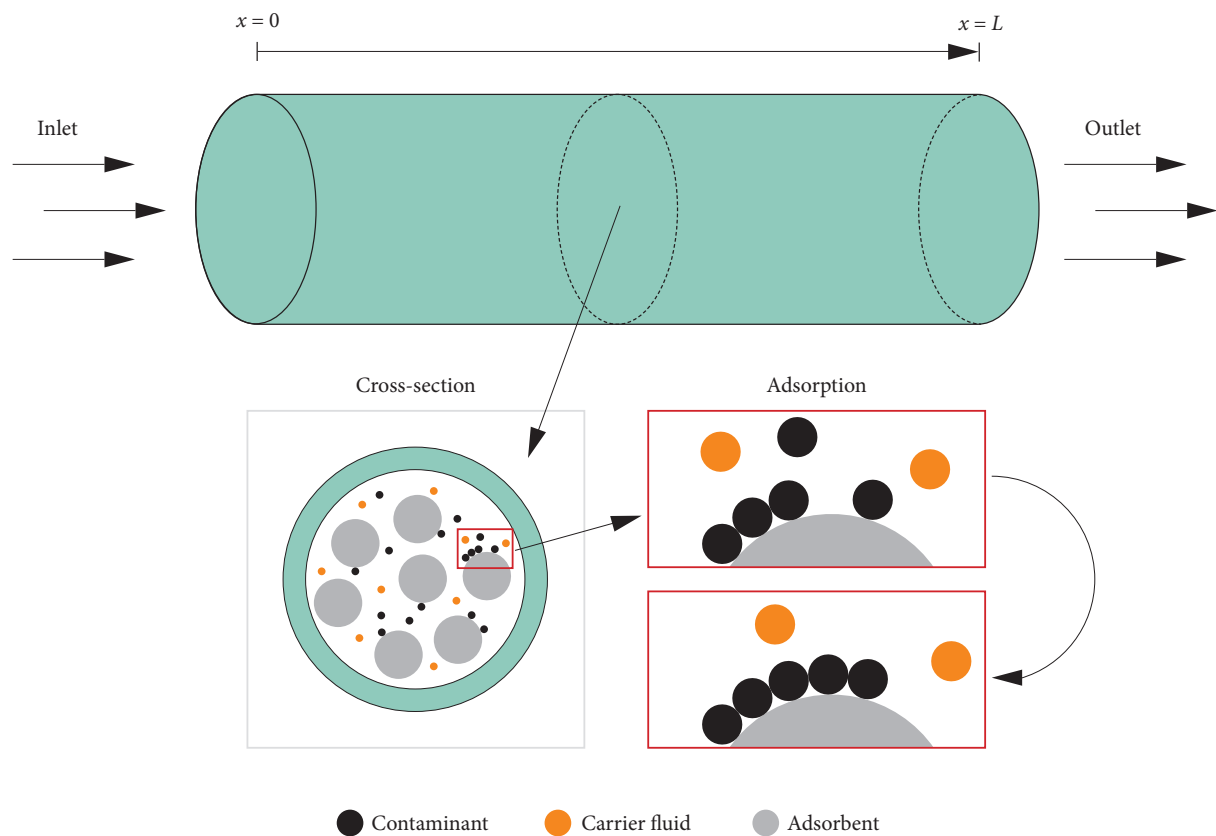


Figure 1: Sketch of an adsorption column. The contaminated fluid enters the column through the inlet (at $x = 0$ in the illustration). As the fluid flows toward the outlet, contaminant molecules adhere to the surfaces of the adsorbent material. Clean fluid is discharged at the outlet until the adsorbent reaches its saturation point.

to develop a three-dimensional model based on partial differential equations that allows for the explicit inclusion of adsorption reactions on the surface of the porous media.

A detailed 3D computational model, like the one developed in this study, is valuable for analyzing the impact of the microstructure on the adsorption process. It can be applied to arbitrary geometries, such as those from computed tomography scans of real columns, to assess its effects in realistic settings. However, the simplicity of 1D models like (1), which allow for approximate analytical solutions of breakthrough curves, remains highly valuable to experimentalists. In [12], the model (1) was derived using a cross-sectional averaging approach, under the assumption that the porosity of the cross-section does not vary along the axial direction. This is a rather restrictive assumption, which we also address in this paper by instead assuming a constant volumetric porosity. In particular, we employ homogenization techniques to derive a 1D model, where the microstructure contribution explicitly appears in the governing equations. We demonstrate that the resulting model is equivalent to (1), thereby validating the results in [12]. Furthermore, we compare the solutions obtained from the detailed 3D model with those from the reduced 1D version and show that they agree remarkably well. This agreement confirms both the robustness of the results in [12] and their suitability for data fitting and predicting filter performance.

This article is structured as follows. In §2, we begin with the derivation and detailed description of a 3D model that captures the evolution of contaminant concentration within the porous media of the filter, accounting for adsorption occurring at the adsorbent surfaces. In §3, we apply asymptotic homogenization techniques to simplify the original 3D model. The effects of the complex microstructure are encapsulated in a single dispersion term, and the adsorption boundary condition is incorporated as a sink term in a reaction-diffusion equation. This new model, defined over the filter's domain, represents a significant simplification of the original formulation. We further demonstrate that the solutions of this system depend solely on the axial direction, leading to equations that are equivalent to those in (1). In §4, we conduct numerical simulations to compare the results of the complete 3D model with the simplified 1D model, showing excellent agreement in the breakthrough curves produced by both approaches. Finally, §5 summarizes the conclusions of this work.

2 A 3D mathematical model for column adsorption

In this section, we present a mathematical model for an adsorption column filled with impermeable particles of arbitrary size and shape. The column is assumed to have a cylindrical geometry, with the adsorbent material randomly distributed throughout its interior (see Figure 2). Contaminated fluid is injected at the inlet, and as it flows through the reactor, the contaminant molecules are adsorbed onto the particles surfaces, resulting in the release of clean fluid at the outlet. We assume that the contaminant concentration is sufficiently low to remain far from saturation, allowing us to neglect any mass loss effects. Additionally, and as explained in [10], in most settings the process can be assumed to be isothermal and thus we neglect any heat transfer effects.

The interior domain of the column, Ω , is composed of two parts: a solid region occupied by the impermeable solid grains, denoted by Ω_s , and the surrounding space through which the

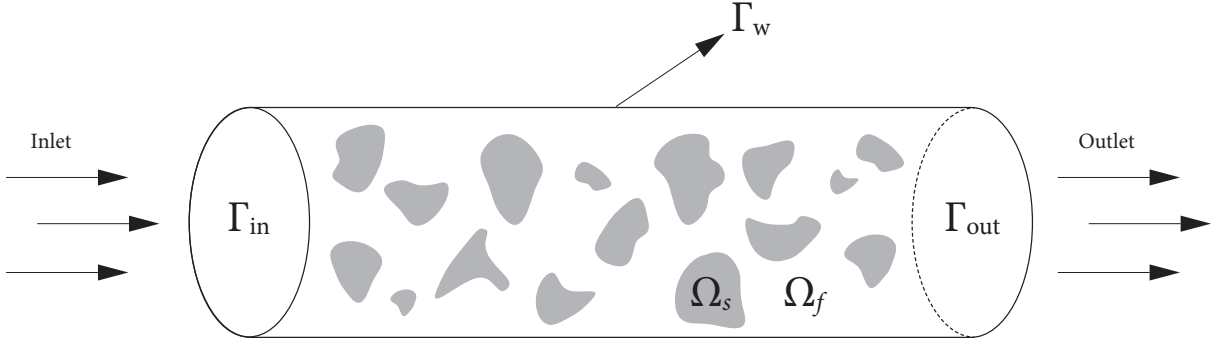


Figure 2: Sketch of an adsorption column with adsorbent particles of different sizes and shapes and domain's description.

fluid flows, denoted by Ω_f . The porosity is the void fraction of the column, that is

$$\phi = \frac{|\Omega_f|}{|\Omega_f| + |\Omega_s|}.$$

The equation for the concentration of contaminant in the fluid region, $c(\mathbf{x}, t)$ (mols of contaminant per unit volume), corresponds to a standard advection-diffusion equation,

$$\nabla \cdot (\mathcal{D} \nabla c - \mathbf{u}c) = \frac{\partial c}{\partial t}, \quad \mathbf{x} \in \Omega_f, \quad (2a)$$

where \mathcal{D} is the brownian diffusion. The adsorption reaction, which takes place at the grain's surfaces, is introduced in the model as follows. Denoting by \mathbf{n}_s the outward normal vector at the solid grains, the flux of contaminant entering the solid region is

$$-\mathbf{n}_s \cdot (\mathcal{D} \nabla c - \mathbf{u}c) |\partial \Omega_s|.$$

This must be equal to the concentration of contaminant (in mols of contaminant per unit volume) retained at the solid region, $|\Omega_s| \partial c^{\text{ad}} / \partial t$. It is common practice to express the adsorption rate in terms of the nondimensional contaminant density given by the ratio of the adsorbed mass over the mass of the bulk adsorbent material m^{ad}/m_b . This magnitude can be averaged over a cross section (as done in [12]) or per unit volume to relate it with c^{ad} , which motivates the following definition for the adsorbed fraction of contaminant

$$q(\mathbf{x}, t) = \frac{|\Omega_s| c^{\text{ad}}(\mathbf{x}, t)}{\rho_b (|\Omega_s| + |\Omega_f|)} = \frac{(1 - \phi) c^{\text{ad}}(\mathbf{x}, t)}{\rho_b}, \quad (2b)$$

where ρ_b is the density of the bulk adsorbent material (defined as the ratio of the mass of adsorbent to the column volume), which is assumed to be constant along the column. Therefore, the boundary condition at the surface of the solid grains can be written like

$$-\mathbf{n}_s \cdot (\mathcal{D} \nabla c - \mathbf{u}c) |\partial \Omega_s| = |\Omega_s| \frac{\rho_b}{1 - \phi} \frac{\partial q}{\partial t}, \quad \mathbf{x} \in \partial \Omega_s. \quad (2c)$$

Equation (2c) must be coupled to a dynamical condition for the adsorption rate at the grain's surface. Following the work in [12] we consider the model that is most consistent with the kinetics of the physicochemical reactions that take place in adsorption processes

$$\frac{\partial q}{\partial t} = k_{\text{ad}} c^m (q_{\text{max}} - q)^n - k_{\text{de}} q^n, \quad \mathbf{x} \in \partial\Omega_s, \quad (2d)$$

where k_{ad} and k_{de} are the adsorption and desorption rates and q_{max} is the maximum concentration fraction that the adsorbent can retain. The adsorption and desorption rates are known to depend on the temperature and flow velocity, which in this work are assumed to be constant.

At the inlet, Γ_{in} , we assume a Dankwert condition (see [20]), and at the outlet, Γ_{out} , we simply impose a no-flux condition (see [21] for a justification of the convenience of this simplification) and of course impermeability of the reactor's wall must be imposed:

$$(\mathbf{u}c - \mathcal{D}\nabla c) \cdot \mathbf{n}_{\text{in}} = \mathbf{n}_{\text{in}} \cdot \mathbf{u}c_{\text{in}}, \quad \mathbf{x} \in \Gamma_{\text{in}}, \quad (2e)$$

$$\mathcal{D}\nabla c \cdot \mathbf{n}_{\text{out}} = 0, \quad \mathbf{x} \in \Gamma_{\text{out}}, \quad (2f)$$

$$\nabla c \cdot \mathbf{n}_{\text{w}} = 0, \quad \mathbf{x} \in \Gamma_{\text{w}}, \quad (2g)$$

where $\mathbf{n}_{\text{in}} = (-1, 0, 0)$, $\mathbf{n}_{\text{out}} = (1, 0, 0)$, \mathbf{n}_{w} is the radial unitary vector, and $\Gamma_{\text{in}}, \Gamma_{\text{out}}$ and Γ_{w} are as illustrated in Figure 2. Assuming a Stokes flow with an incompressible fluid and a vanishing velocity condition at the grain's and wall's surfaces the fluid equations for the pressure, $p(\mathbf{x}, t)$, and velocity, $\mathbf{u}(\mathbf{x}, t)$ read

$$-\nabla p + \mu \nabla^2 \mathbf{u} = 0, \quad \mathbf{x} \in \Omega_f, \quad (3a)$$

$$\nabla \cdot \mathbf{u} = 0, \quad \mathbf{x} \in \Omega_f, \quad (3b)$$

$$\mathbf{u} = 0, \quad \mathbf{x} \in \partial\Omega_s \cup \Gamma_{\text{w}}, \quad (3c)$$

$$\mathbf{u} = u_{\text{in}} \mathbf{e}_1, \quad \mathbf{x} \in \Gamma_{\text{in}}, \quad (3d)$$

where \mathbf{e}_1 is the unitary vector in the axial direction. Equation (3a) is the equation for a Stokes flow, equation (3b) accounts for the incompressibility of the fluid, equation (3c) is the no-slip condition of the fluid at the grain's and wall's surfaces and (3d) imposes a constant inlet velocity in the axial direction. We note that the flow equations (3) can be solved independently of the concentration equations (2).

3 Derivation of a one-dimensional model using homogenization

In [10] and [12], the authors perform a section average of equation (2a) and, by taking into account that there is a mass loss through the solid grains' surfaces, an equation for the mean concentration in each section is derived. In those derivations the dispersion coefficient (D in equation (1)) is not directly connected with the microstructure and it is treated as a fitting parameter. In fact, in most experimental settings, the effective diffusion ends up being small enough to be neglected, as the authors show in [10] and [12]. They also assume that the porosity in each cross section, defined as the area occupied by the fluid divided by the total area, is constant.

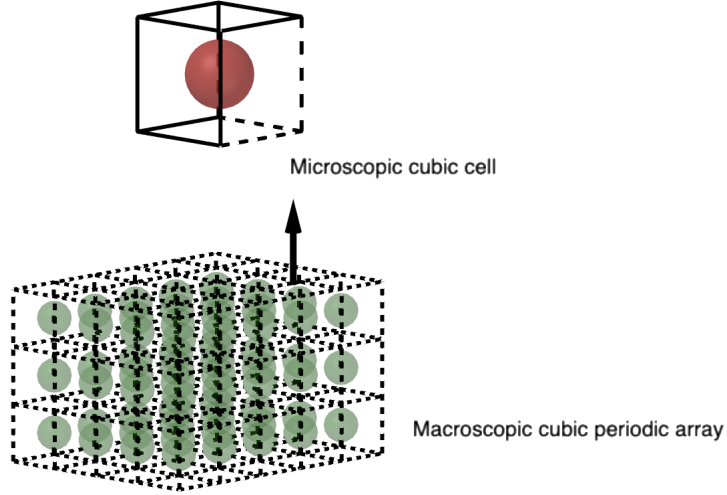


Figure 3: Grains of adsorbent material in a periodic cubic arrangement. The spheres are separated by distances of size ℓ . Rescaled microscopic unitary cubic cell.

In what follows we assume that the domain is composed of a set of periodically arranged spherical grains whose centres are separated by a distance of size $\ell \ll \mathcal{L}$ (see Figure 3), where \mathcal{L} is the adsorption length scale that will be determined later. We also define the small parameter $\epsilon = \ell/\mathcal{L}$. We note that $|\Omega_s|$ is the union of a set of spheres with the same radius, and therefore $|\Omega_s|/|\partial\Omega_s| = r/3 < \ell/3 = \mathcal{O}(\epsilon)$ is the inverse of the specific surface area of a spherical grain. We also define the following non-dimensional variables

$$\mathbf{x} = \mathcal{L}\hat{\mathbf{x}}, \quad t = \tau\hat{t}, \quad c = c_{\text{in}}\hat{c}, \quad q = q_{\text{max}}\hat{q}, \quad \mathbf{u} = u_{\text{in}}\hat{\mathbf{u}}, \quad (4)$$

where τ is the adsorption time scale that is given by

$$\tau = \frac{1}{k_{\text{ad}}c_{\text{in}}^m q_{\text{max}}^{n-1}},$$

\mathcal{L} is the corresponding length scale which will be determined later, and q_{max} is the maximum concentration that the adsorbent can retain. Dropping the hats and using the following constants,

$$\text{Da} = \frac{\mathcal{L}}{u_{\text{in}}\tau}, \quad \text{Pe}^{-1} = \frac{\mathcal{D}}{\mathcal{L}u_{\text{in}}}, \quad \beta = \frac{|\Omega_s|}{|\partial\Omega_s|\epsilon} \frac{q_{\text{max}}\rho_b\mathcal{L}}{c_{\text{in}}u_{\text{in}}\tau}, \quad \delta = \frac{k_{\text{de}}}{k_{\text{ad}}c_{\text{in}}^m q_{\text{max}}^{n-1}}, \quad p = \frac{u_{\text{in}}\mu}{\epsilon^2\mathcal{L}}\hat{p},$$

yields the non-dimensional version of equations (2):

$$\nabla \cdot (\text{Pe}^{-1} \nabla c - \mathbf{u}c) = \text{Da} \frac{\partial c}{\partial t}, \quad \mathbf{x} \in \Omega_f, \quad (5a)$$

$$\mathbf{n}_s \cdot (\text{Pe}^{-1} \nabla c - \mathbf{u}c) = -\epsilon\beta \frac{\partial q}{\partial t}, \quad \mathbf{x} \in \partial\Omega_s, \quad (5b)$$

$$c^m(q_{\text{max}} - q)^n - \delta q^n = \frac{\partial q}{\partial t}, \quad \mathbf{x} \in \partial\Omega_s, \quad (5c)$$

$$(\mathbf{u}c - \text{Pe}^{-1} \nabla c) \cdot \mathbf{n}_{\text{in}} = \mathbf{n}_{\text{in}} \cdot \mathbf{u}, \quad \mathbf{x} \in \Gamma_{\text{in}}, \quad (5d)$$

$$\mathbf{n}_{\text{out}} \cdot \nabla c = 0, \quad \mathbf{x} \in \Gamma_{\text{out}}, \quad (5e)$$

$$\nabla c \cdot \mathbf{n}_w = 0, \quad \mathbf{x} \in \Gamma_w \quad (5f)$$

where the operator ∇ applies to the rescaled variable \mathbf{x} and the domains are the corresponding rescaled domains. As for the fluid equations, the non-dimensional form of equations (3) reads

$$-\nabla p + \epsilon^2 \nabla^2 \mathbf{u} = 0, \quad \mathbf{x} \in \Omega_f \quad (6a)$$

$$\nabla \cdot \mathbf{u} = 0, \quad \mathbf{x} \in \Omega_f, \quad (6b)$$

$$\mathbf{u} = 0, \quad \mathbf{x} \in \partial\Omega_s \cup \Gamma_w. \quad (6c)$$

3.1 Homogenization

In what follows we will derive a set of equations on a simpler macroscale domain whose properties capture the effect of the actual microscopic geometry. To do so we use the method of multiple scales (MMS) and start by introducing a microscale variable, $\mathbf{y} := \mathbf{x}/\epsilon$, and as is standard in the MMS, assume that the macroscopic variable, \mathbf{x} , and the microscopic one, \mathbf{y} , are independent. Therefore, we continue by writing $c(\mathbf{x}, t) = c(\mathbf{x}, \mathbf{y}, t)$, $c^{\text{ad}}(\mathbf{x}, t) = c^{\text{ad}}(\mathbf{x}, \mathbf{y}, t)$, $\mathbf{u}(\mathbf{x}, t) = \mathbf{u}(\mathbf{x}, \mathbf{y}, t)$, and $p(\mathbf{x}, t) = p(\mathbf{x}, \mathbf{y}, t)$. The microscale variable, \mathbf{y} , is defined in a unitary cubic domain, $[-1/2, 1/2]^3 = \omega_f \cup \omega_s$, being $\omega_s = \{[-1/2, 1/2]^3 \setminus |\mathbf{y}| \leq r/\ell := \nu\}$ the particle's domain and ω_f the fluid region, and we allow both to depend on the macroscopic variable. We note that $|\omega_f| = \phi$. The boundary of the fluid region in the cubic cell is given by $\partial\omega_f = \partial\omega_s \cup \gamma$, where $\partial\omega_s = \{|\mathbf{y}| = \nu\}$ is the surface boundary of the grain and $\gamma = \partial([-1/2, 1/2]^3)$. The gradient operator in the new variables (\mathbf{x}, \mathbf{y}) reads

$$\nabla = \nabla_{\mathbf{x}} + \frac{1}{\epsilon} \nabla_{\mathbf{y}},$$

and so equations (5) for the contaminant concentration, $c(\mathbf{x}, \mathbf{y}, t)$, and for the amount being already adsorbed, $c^{\text{ad}}(\mathbf{x}, \mathbf{y}, t)$, read

$$\text{Pe}^{-1} \left(\nabla_{\mathbf{x}}^2 c + \frac{1}{\epsilon} \nabla_{\mathbf{x}} \nabla_{\mathbf{y}} c + \frac{1}{\epsilon} \nabla_{\mathbf{y}} \nabla_{\mathbf{x}} c + \frac{1}{\epsilon^2} \nabla_{\mathbf{y}}^2 c \right) \quad (7a)$$

$$-\nabla_{\mathbf{x}} \cdot (\mathbf{u}c) - \frac{1}{\epsilon} \nabla_{\mathbf{y}} \cdot (\mathbf{u}c) = \text{Da} \frac{\partial c}{\partial t}, \quad \mathbf{y} \in \omega_f, \quad (7b)$$

$$\mathbf{n}_s(\mathbf{x}) \left(\text{Pe}^{-1} \nabla_{\mathbf{x}} c + \frac{\text{Pe}^{-1}}{\epsilon} \nabla_{\mathbf{y}} c - \mathbf{u}c \right) = -\epsilon\beta \frac{\partial q}{\partial t}, \quad |\mathbf{y}| = \nu, \quad (7c)$$

$$c(\mathbf{x}, \mathbf{y}, t), c^{\text{ad}}(\mathbf{x}, \mathbf{y}, t), \mathbf{u}(\mathbf{x}, \mathbf{y}, t), \mathbf{y}\text{-periodic}, \quad \mathbf{y} \in \omega_f.$$

The flow equations, which can be solved independently of the concentration equations, read

$$-\nabla_{\mathbf{x}} p - \frac{1}{\epsilon} \nabla_{\mathbf{y}} p + \epsilon^2 \nabla_{\mathbf{x}}^2 \mathbf{u} + \epsilon \nabla_{\mathbf{x}} \nabla_{\mathbf{y}} \mathbf{u} + \epsilon \nabla_{\mathbf{y}} \nabla_{\mathbf{x}} \mathbf{u} + \nabla_{\mathbf{y}}^2 \mathbf{u} = 0, \quad \mathbf{y} \in \omega_f, \quad (8a)$$

$$\nabla_{\mathbf{x}} \cdot \mathbf{u} + \frac{1}{\epsilon} \nabla_{\mathbf{y}} \cdot \mathbf{u} = 0 \quad \mathbf{y} \in \omega_f, \quad (8b)$$

$$\mathbf{u} = 0, \quad |\mathbf{y}| = \nu \quad (8c)$$

$$p(\mathbf{x}, \mathbf{y}, t), \mathbf{u}(\mathbf{x}, \mathbf{y}, t), \mathbf{y}\text{-periodic}, \quad \mathbf{y} \in \omega_f,$$

We thus proceed and introduce the expansions

$$p(\mathbf{x}, \mathbf{y}, t), \sim p_0(\mathbf{x}, \mathbf{y}, t) + \epsilon p_1(\mathbf{x}, \mathbf{y}, t) + \dots,$$

$$\mathbf{u}(\mathbf{x}, \mathbf{y}, t) \sim \mathbf{u}_0(\mathbf{x}, \mathbf{y}, t) + \epsilon \mathbf{u}_1(\mathbf{x}, \mathbf{y}, t) + \dots,$$

as $\epsilon \rightarrow 0$ and obtain, at leading order,

$$\nabla_{\mathbf{y}} p_0 = 0, \quad \mathbf{y} \in \omega_\epsilon, \quad \text{and } p_0 \text{ is } \mathbf{y} \text{-periodic,} \quad (9)$$

whose only possible solution is $p_0(\mathbf{x}, \mathbf{y}, t) = p_0(\mathbf{x}, t)$. The order one terms give,

$$-\nabla_{\mathbf{y}} p_1 + \nabla_{\mathbf{y}}^2 \mathbf{u}_0 = \nabla_{\mathbf{x}} p_0, \quad \mathbf{y} \in \omega_f, \quad (10a)$$

$$\nabla_{\mathbf{y}} \cdot \mathbf{u}_0 = 0, \quad \mathbf{y} \in \omega_f, \quad (10b)$$

$$\mathbf{u}_0 = 0, \quad |\mathbf{y}| = \nu, \quad (10c)$$

$\mathbf{u}_0(\mathbf{x}, \mathbf{y}, t), p_1(\mathbf{x}, \mathbf{y}, t)$ are \mathbf{y} -periodic,

whose solution can be written like

$$\mathbf{u}_0(\mathbf{x}, \mathbf{y}, t) = - \sum_{j=1}^3 \left(\mathbf{K}_j(\mathbf{x}, \mathbf{y}) \frac{\partial p_0(\mathbf{x}, t)}{\partial x_j} \right), \quad (11a)$$

$$p_1(\mathbf{x}, \mathbf{y}, t) = - \sum_{j=1}^3 \left(\Pi_j(\mathbf{x}, \mathbf{y}) \frac{\partial p_0(\mathbf{x}, t)}{\partial x_j} \right) + \tilde{p}(\mathbf{x}, t), \quad (11b)$$

where $\tilde{p}(\mathbf{x}, t)$ is an arbitrary function independent of \mathbf{y} which will not play any role in the leading order approximation. Denoting by δ_{ij} the Delta Kronecker function ($\delta_{ij} = 1$ if $j = i$ and 0 otherwise), $\Pi_j, \mathbf{K}_j = (K_{j1}, K_{j2}, K_{j3})$ are the solutions of

$$\delta_{ij} - \frac{\partial \Pi_i}{\partial y_j} + \nabla_{\mathbf{y}}^2 K_{ij} = 0, \quad \mathbf{y} \in \omega_f, \quad (12a)$$

$$\frac{\partial K_{j1}}{\partial y_1} + \frac{\partial K_{j2}}{\partial y_2} + \frac{\partial K_{j3}}{\partial y_3} = 0, \quad \mathbf{y} \in \omega_f, \quad (12b)$$

$$K_{ji} = 0, \quad |\mathbf{y}| = \nu, \quad (12c)$$

and

$$\Pi_j, K_{ij} \quad \mathbf{y}\text{-periodic, and } \int_{\omega_f} \Pi_j(\mathbf{x}, \mathbf{y}), d\mathbf{y} = \int_{\omega_f} K_{ij}(\mathbf{x}, \mathbf{y}), d\mathbf{y} = 0, \quad (12d)$$

for $i, j = 1..3$, which have unique solutions. The (constant) interstitial velocity term in equation (1) corresponds to the intrinsic average given by

$$\mathbf{u}(\mathbf{x}, t) = \frac{1}{|\omega_f|} \int_{\omega_f} \mathbf{u}_0(\mathbf{x}, \mathbf{y}, t) d\mathbf{y} = \frac{1}{\phi} \int_{\omega_f} \mathbf{u}_0(\mathbf{x}, \mathbf{y}, t) d\mathbf{y}. \quad (13)$$

Integrating (11a) over the cell fluid domain,

$$\int_{\omega_f} \mathbf{u}_0(\mathbf{x}, \mathbf{y}, t) d\mathbf{y} = -\mathcal{K} \nabla_{\mathbf{x}} p_0(\mathbf{x}, t), \quad (14)$$

where $\mathcal{K} = (k_{ij})$ is a symmetric 3 dimensional matrix whose entries are given by

$$k_{ij}(\mathbf{x}) = \int_{\omega_f} K_{ij}(\mathbf{x}, \mathbf{y}) d\mathbf{y},$$

that is actually Darcy's law for the macroscopic model. As for the concentration problem, we do as before and we introduce the expansion $c(\mathbf{x}, \mathbf{y}, t) \sim c_0(\mathbf{x}, \mathbf{y}, t) + \epsilon c_1(\mathbf{x}, \mathbf{y}, t) + \epsilon^2 c_2(\mathbf{x}, \mathbf{y}, t) + \dots$, which substituting in (7) gives, to leading order,

$$\nabla_{\mathbf{y}}^2 c_0 = 0, \quad \mathbf{y} \in \omega_f \quad (15a)$$

$$\mathbf{n}_s(\mathbf{x}) \cdot \nabla_{\mathbf{y}} c_0 = 0, \quad |\mathbf{y}| = \nu \quad (15b)$$

$$c_0(x, y, t) \text{ is } \mathbf{y}\text{-periodic,}$$

whose solution is independent of the microscopic variable \mathbf{y} , that is $c_0(\mathbf{x}, \mathbf{y}, t) = c_0(\mathbf{x}, t)$. Continuing to the following order the first order approximation of the concentration is found to satisfy

$$\nabla_{\mathbf{y}}^2 c_1 = 0, \quad \mathbf{y} \in \omega_f \quad (16a)$$

$$\mathbf{n}_s(\mathbf{x}) \cdot \nabla_{\mathbf{y}} c_1 = -\mathbf{n}_s(\mathbf{x}) \cdot \nabla_{\mathbf{x}} c_0, \quad |\mathbf{y}| = \nu \quad (16b)$$

$$c_1(x, y, t) \text{ is } \mathbf{y}\text{-periodic.}$$

To solve (16) we note that:

$$\nabla_{\mathbf{x}} c_0(\mathbf{x}, t) = \sum_{j=1}^3 \left(\mathbf{e}_j \frac{\partial c_0(\mathbf{x}, t)}{\partial x_j} \right),$$

so one can write

$$c_1(\mathbf{x}, \mathbf{y}, t) = \tilde{c}(\mathbf{x}, t) - \sum_{j=1}^3 \left(\xi_j(\mathbf{x}, \mathbf{y}) \frac{\partial c_0(\mathbf{x}, t)}{\partial x_j} \right), \quad (17)$$

where $\tilde{c}(\mathbf{x}, t)$ is an arbitrary function independent of \mathbf{y} that will not play any role in the leading order approximation, and where the functions $\xi_j(\mathbf{x}, \mathbf{y})$ satisfy the following cell problem:

$$\nabla_{\mathbf{y}}^2 \xi_j = 0, \quad \mathbf{y} \in \omega_f, \quad (18a)$$

$$\mathbf{n}_s(\mathbf{x}) \nabla_{\mathbf{y}} \xi_j = \frac{y_j}{\nu}, \quad |\mathbf{y}| = \nu, \quad (18b)$$

$$\xi_j \text{ is } \mathbf{y}\text{-periodic and } \int_{\omega_f} \xi_j(\mathbf{x}, \mathbf{y}) \, d\mathbf{y} = 0. \quad (18c)$$

Continuing to the next order, the equation for the concentration yields

$$\text{Pe}^{-1} (\nabla_{\mathbf{x}}^2 c_0 + 2\nabla_{\mathbf{x}} \nabla_{\mathbf{y}} c_1 + \nabla_{\mathbf{y}}^2 c_2) - \nabla_{\mathbf{x}}(\mathbf{u}_0 c_0) - \nabla_{\mathbf{y}}(\mathbf{u}_0 c_1 + \mathbf{u}_1 c_0) = \text{Da} \frac{\partial c_0}{\partial t}, \quad \mathbf{y} \in \omega_f, \quad (19a)$$

$$\mathbf{n}_s (\text{Pe}^{-1} (\nabla_{\mathbf{x}} c_1 + \nabla_{\mathbf{y}} c_2) - \mathbf{u}_0 c_1 - \mathbf{u}_1 c_0) = -\beta \frac{\partial q}{\partial t}, \quad |\mathbf{y}| = \nu, \quad (19b)$$

$$c_2 \text{ is } \mathbf{y}\text{-periodic}$$

and c_2 is \mathbf{y} -periodic. We now integrate equations (19) over the cell fluid region, ω_f , which gives:

$$\begin{aligned} \nabla_{\mathbf{x}} \cdot \left[\int_{\omega_f} (\text{Pe}^{-1} (\nabla_{\mathbf{x}} c_0 + \nabla_{\mathbf{y}} c_1) - \mathbf{u}_0 c_0) \, d\mathbf{y} \right] \\ + \int_{\omega_f} \nabla_{\mathbf{y}} \cdot (\text{Pe}^{-1} (\nabla_{\mathbf{x}} c_1 + \nabla_{\mathbf{y}} c_2) - (\mathbf{u}_0 c_1 + \mathbf{u}_1 c_0)) \, d\mathbf{y} = \text{Da} \int_{\omega_f} \frac{\partial c_0}{\partial t} \, d\mathbf{y}. \end{aligned}$$

Using the Gauss-Green theorem along with the boundary and periodicity conditions this equation reduces to

$$\nabla_{\mathbf{x}} \cdot \left[\int_{\omega_f} (\text{Pe}^{-1}(\nabla_{\mathbf{x}}c_0 + \nabla_{\mathbf{y}}c_1) - \mathbf{u}_0c_0) \, d\mathbf{y} \right] - \beta \int_{|\mathbf{y}|=\nu} \frac{\partial q}{\partial t} \, d\ell = \text{Da} |\omega_f| \frac{\partial c_0}{\partial t}. \quad (20)$$

Dividing by $|\omega_f| = \phi$ and using (13) and (17), equation (20) reads

$$\nabla_{\mathbf{x}} \cdot \left[\text{Pe}^{-1} \left(\nabla_{\mathbf{x}}c_0 - \sum_{j=1}^3 \frac{\partial c_0}{\partial x_j} \frac{1}{\phi} \int_{\omega_f} \nabla_{\mathbf{y}}\omega_j(\mathbf{x}, \mathbf{y}) \, d\mathbf{y} \right) \right] - \nabla_{\mathbf{x}} \cdot (c_0\mathbf{u}) = \frac{\beta}{\phi} \int_{|\mathbf{y}|=\nu} \frac{\partial q}{\partial t} \, d\ell + \text{Da} \frac{\partial c_0}{\partial t}.$$

In [12], the authors obtain equations (1) in terms of an intrinsic average over each cross section. Therefore, denoting the intrinsic average for the concentration as $c(\mathbf{x}, t)$,

$$c(\mathbf{x}, t) = \frac{1}{\phi} \int_{\omega_f} c(\mathbf{x}, \mathbf{y}, t) \, d\mathbf{y} \sim \frac{1}{\phi} \int_{\omega_f} c_0(\mathbf{x}, t) \, d\mathbf{y} = c_0(\mathbf{x}, t). \quad (21)$$

We note that q is a magnitude that represents the amount of contaminant trapped at each grain, so it is intrinsically independent of \mathbf{y} . Therefore,

$$\frac{\beta}{\phi} \int_{|\mathbf{y}|=\nu} \frac{\partial q}{\partial t} \, d\ell = \frac{\beta |\partial\omega_s|}{\phi} \frac{\partial q}{\partial t} = \frac{|\Omega_s| |\partial\omega_s|}{\epsilon |\partial\Omega_s|} \frac{q_{\max} \rho_b \mathcal{L}}{(1-\phi)c_{\text{in}} u_{\text{in}} \phi \tau} \frac{\partial q}{\partial t} = \frac{q_{\max} \rho_b \mathcal{L}}{c_{\text{in}} u_{\text{in}} \phi \tau} \frac{\partial q}{\partial t}.$$

We recall that \mathcal{L} is the adsorption length scale which has not been determined yet. Choosing

$$\mathcal{L} = \frac{c_{\text{in}} u_{\text{in}} \phi}{q_{\max} \rho_b} \tau,$$

and defining the tensor $\mathcal{A}_{\text{disp}} = (d_{ij}) : \Omega \rightarrow \mathbb{R}^{3 \times 3}$ where, $d_{ij} : \Omega \rightarrow \mathbb{R}$, with $i, j = 1, \dots, 3$ and

$$d_{ij} = \text{Pe}^{-1} \int_{\omega_f} \left(\delta_{ij} - \frac{1}{\phi} \frac{\partial \omega_j}{\partial y_i} \right) \, d\mathbf{y},$$

yields,

$$\nabla_{\mathbf{x}} \cdot (\text{Pe}^{-1} \mathcal{A}_{\text{disp}} \nabla_{\mathbf{x}}c_0 - c_0\mathbf{u}) = \text{Da} \frac{\partial c_0}{\partial t} + \frac{\partial q}{\partial t}, \quad \mathbf{x} \in \Omega. \quad (22)$$

In this particular setting, $\mathcal{A}_{\text{disp}}$ is a diagonal matrix:

$$d_{ij} = 0, \quad \text{if } i \neq j, \text{ and } d_{11} = d_{22} = d_{33} = d, \quad (23)$$

so one can define an effective Péclet number:

$$\text{Pe}_{\text{eff}}^{-1} = d \text{Pe}^{-1} = \frac{d\mathcal{D}}{\mathcal{L}u_{\text{in}}} = \frac{D}{\mathcal{L}u_{\text{in}}},$$

where D is the effective dispersion of the media which incorporates the effect of the microstructure. Therefore, to leading order, one has that at the macroscopic scale,

$$\text{Pe}_{\text{eff}}^{-1} \nabla^2 c_0 - \nabla \cdot (c_0\mathbf{u}) = \text{Da} \frac{\partial c_0}{\partial t} + \frac{\partial q}{\partial t}, \quad \mathbf{x} \in \Omega, \quad (24a)$$

$$c_0^m (q_{\max} - q)^n - \delta q^n = \frac{\partial q}{\partial t}, \quad \mathbf{x} \in \Omega. \quad (24b)$$

We note that $\text{Pe}_{\text{eff}}^{-1}$ now depends on the dispersion coefficient which depends on the brownian diffusion, \mathcal{D} and on the media porosity, ϕ . As for the velocity, combining (13) and (14), it satisfies Darcy's law given by

$$\mathbf{u}(\mathbf{x}, t) = -\frac{1}{\phi} \mathcal{K} \nabla_{\mathbf{x}} p_0(\mathbf{x}, t). \quad (24c)$$

3.2 Reduction to a one-dimensional problem

In the previous section we have reduced the problem (5) for the evolution of the contaminant concentration on a complex domain to

$$\text{Pe}_{\text{eff}}^{-1} \nabla^2 c - \nabla \cdot (c\mathbf{u}) = \text{Da} \frac{\partial c}{\partial t} + \frac{\partial q}{\partial t}, \quad \mathbf{x} \in \Omega, \quad (25a)$$

$$c^m (q_{\text{max}} - q)^n - \delta q^n = \frac{\partial q}{\partial t}, \quad \mathbf{x} \in \Omega, \quad (25b)$$

$$(\mathbf{u}c - \text{Pe}_{\text{eff}}^{-1} \nabla c) \cdot \mathbf{n}_{\text{in}} = \mathbf{n}_{\text{in}} \cdot \mathbf{u}, \quad \mathbf{x} \in \Gamma_{\text{in}}, \quad (25c)$$

$$\mathbf{n}_{\text{out}} \cdot \nabla c = 0, \quad \mathbf{x} \in \Gamma_{\text{out}}, \quad (25d)$$

$$\nabla c \cdot \mathbf{n}_{\text{w}} = 0, \quad \mathbf{x} \in \Gamma_{\text{w}} \quad (25e)$$

where Ω is the cylinder of (non-dimensional) length L , and (non-dimensional) radius R , and where

$$\mathbf{u}(\mathbf{x}, t) = -\frac{1}{\phi} \mathcal{K} \nabla_{\mathbf{x}} p_0(\mathbf{x}, t).$$

We note that the velocity goes only in the axial direction since the non dimensional form of equation (3d) provides $\mathbf{u} = \mathbf{e}_1$ at Γ_{in} . Therefore, if the pressure drop is constant, one finds $\mathbf{u} = \mathbf{e}_1$ for all $\mathbf{x} \in \Omega$. Under these conditions, the symmetry of the domain forces c and q to depend only on the axial and radial variables, x, r , so the system (25) can be written like

$$\text{Pe}_{\text{eff}}^{-1} \left(\frac{\partial^2 c}{\partial x^2} + \frac{\partial^2 c}{\partial r^2} + \frac{1}{r} \frac{\partial c}{\partial r} \right) - \frac{\partial c}{\partial x} = \text{Da} \frac{\partial c}{\partial t} + \frac{\partial q}{\partial t}, \quad x \in (0, L), r \in (0, R), t > 0, \quad (26a)$$

$$c^m (q_{\text{max}} - q)^n - \delta q^n = \frac{\partial q}{\partial t}, \quad x \in (0, L), r \in (0, R), t > 0, \quad (26b)$$

$$\left(c - \text{Pe}_{\text{eff}}^{-1} \frac{\partial c}{\partial x} \right) \Big|_{x=0^-} = 1, \quad \frac{\partial c}{\partial x} \Big|_{x=L^-} = 0, \quad \frac{\partial c}{\partial r} \Big|_{r=R} = 0, t > 0. \quad (26c)$$

We note that equations (26) have solutions where both r and q are independent of the radial variable r . In fact, given the geometry of the problem and the axiality of the fluid velocity, it seems natural to expect c and q to vary only in the axial direction. Therefore, the system (26) reads

$$\text{Pe}_{\text{eff}}^{-1} \frac{\partial^2 c}{\partial x^2} - \frac{\partial c}{\partial x} = \text{Da} \frac{\partial c}{\partial t} + \frac{\partial q}{\partial t}, \quad x \in (0, L), t > 0, \quad (27a)$$

$$c^m (q_{\text{max}} - q)^n - \delta q^n = \frac{\partial q}{\partial t}, \quad x \in (0, L), t > 0, \quad (27b)$$

$$\left(c - \text{Pe}_{\text{eff}}^{-1} \frac{\partial c}{\partial x} \right) \Big|_{x=0^-} = 1, \quad \frac{\partial c}{\partial x} \Big|_{x=L^-} = 0, \quad t > 0, \quad (27c)$$

The dimensionless problem (27) can be rewritten in dimensional form by reverting the change of variables defined in (4), which yields the system (1). Note that the homogenized model and its corresponding 1D reduction were derived for a microstructure consistent in a periodic array of spheres, where the size of the unit cell is much smaller than the adsorption length-scale. This structure might look rather restrictive and far from the actual randomly distributed grains that one finds in real applications. However, in the next section we will show how, even when the arrays are not periodic and the spheres forming the microstructure have moderate sizes comparable with the cylinder radius, the solution of the derived 1D model gives an extremely accurate description of the process, which proves the robustness of the 1D derivation.

4 3D computational experiments and assessment of the averaged 1D model

In this section, we develop computational experiments to: (i) analyse the effect of the microstructure of the porous media in the adsorption process and (ii) assess the capacity of the averaged 1D model to describe the results of the 3D computational experiments. The experiments involve the solution of the 3D model developed in Section 2 on idealized porous structure domains, using operating conditions from real column adsorption experiments extracted from the literature. The results of the computational experiments are then compared to the predictions of the 1D model derived in Section 3.2.

4.1 Computational experiments: parameters and geometries

To build the computational experiments, we take as a reference the column adsorption experiments for CO₂ capture in He-CO₂ mixtures developed in [16]. We focus on the experimental runs performed at low volume fraction of CO₂ in He, in particular the ones where only the 14% of the mixture volume is composed of CO₂, such that the diluted approximation is not challenged. The column geometry and parameter values that enter our 3D model (2)-(3) are listed in Table 1.

Property	Variable	Units	Value
Inlet CO ₂ concentration	c_{in}	mol/m ³	5.436
Max. adsorbed fraction	q_{max}	mol/kg	4.975
Inlet velocity	U_0	m/s	1.69×10^{-3}
Column length	L	cm	16.3
Column radius	R	cm	0.8
Void fraction	ϕ	-	0.52
Adsorbent particle density	ρ_a	kg/m ³	1070
Adsorption constant	k_{ad}	m ³ /mol·s	4.72×10^{-4}
Desorption constant	k_{de}	s ⁻¹	4.31×10^{-2}
Partial orders	m, n	-	1, 1
Gas molecular diffusivity	\mathcal{D}	m ² /s	0.65×10^{-4}
Gas viscosity	μ	Pa·s	1.8×10^{-5}

Table 1: Material properties and operating conditions used in the computational experiments. The first seven properties are extracted from the experiments reported in [16]. The adsorption/desorption constants and the partial orders of the sorption process are extracted from [22]. The last two are from the database [23].

The geometries and the numerical solutions of the 3D model are performed with the commercial software COMSOL Multiphysics. The macroscopic geometry of the computational experiments consists of a cylindrical column of radius R and length L (see values in Table 1). To simulate the microstructure of the porous media, the interior of the column is filled with a dense arrangement of spherical particles following the approach described in [24]. This involves generating a 3D optimal packing of spheres by first looking at the 2D optimal packing of n circles in a larger circle of radius R . By doing this, we can build up the 3D arrangement layer

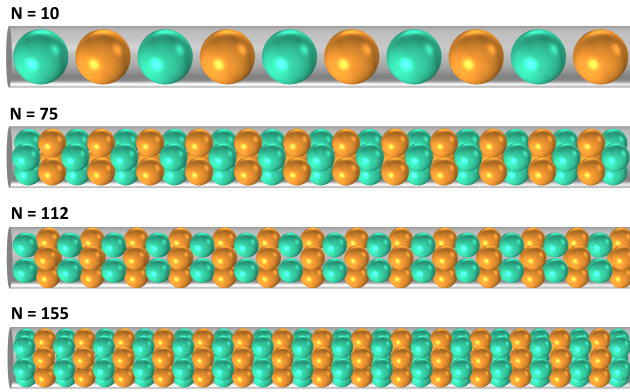


Figure 4: Lateral view of the geometries used in the computational experiments. The inlet of the column is located on the left end, $z = 0$. The different colors indicate different layers. The packing of spheres is formed by a unit cell, a green and a yellow layer, that repeats throughout the column.

by layer, ultimately achieving a dense 3D packing of spheres within the cylinder. We consider 4 different cases, using $n = 1, 3, 4, 5$ spheres per layer, as shown in Figures 4 and 5, which make for a total of $N = 10, 75, 112, 155$ particles within the cylinder, respectively. Once the arrangement is obtained, the radius of the particles is slightly decreased to match the experimental porosity $\phi = 0.52$ in all cases. This also avoids contact between contiguous spheres, thereby preventing potential numerical issues at the contact points. The final particle radius for each case and the corresponding angle of rotation between one layer and the next are summarized in Table 2. Note the case $n = 2$ has not been included since a porosity of $\phi = 0.52$ cannot be achieved for the dimensions R and L of the column used in the present study.

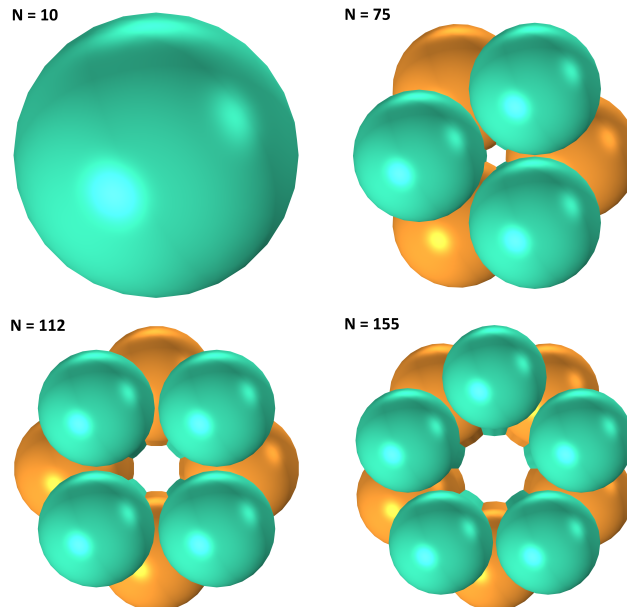


Figure 5: Crosssectional view of the microstructures used in the computational experiments.

The gas mixture flows into the column through the inlet positioned at its left end (see Fig. 4)

N	n	θ	r_p [m]
10	1	-	0.007195
75	3	$\pi/3$	0.0036757
112	4	$\pi/4$	0.0032176
155	5	$\pi/5$	0.0028875

Table 2: Parameter values for the 4 microstructures studied in this work.

at a speed u_{in} and with a contaminant concentration of c_{in} (see Table 1). The gas is allowed to leave the column through the outlet positioned at its right end. While flowing through the free interparticle space inside the column the contaminant is progressively adsorbed on the surface of the particles. When the adsorbed fraction on the particles surface reaches its equilibrium capacity everywhere, the adsorption process ends. At this point, the outlet concentration of contaminant will match the inlet value. In the next section, we describe and discuss the flow velocities and the evolution of the concentration profiles obtained in the four experiments.

4.2 Results of the computational experiments

To solve the 3D model (2)-(3) numerically in COMSOL, we use the *Transport of Diluted Species* option for (2a) and the *Creeping Flow* option for (3a). These equations are solved in Ω_f , i.e. the free space between the spherical particles and the column. Since no pre-established option exists to model adsorption on surfaces, we introduce equation (2d) via the Mathematics module, in particular we use the option *General Form Boundary PDE* to define and solve (2d) on the particles surface, $\partial\Omega_s$. To ensure a high accuracy in the solutions, the meshes are automatically generated with the *Physics-controlled-mesh* option, choosing a *Fine* element size, and a relative tolerance for the time-dependent solver of 10^{-5} . All simulations were run on a workstation equipped with a 13th Gen Intel Core i9-13900K CPU at 3.00 GHz and 128 GB of RAM. Note that in (2)-(3) the velocity equation is decoupled from the concentration and adsorption equations. This allows to solve for the velocity field first and use the solution as input value in the concentration equation, which leads to relatively fast computing times. In particular, the longest runtime occurred for the case $N = 155$, with a computation time of 6 minutes for the velocity field and 38 minutes for the concentration.

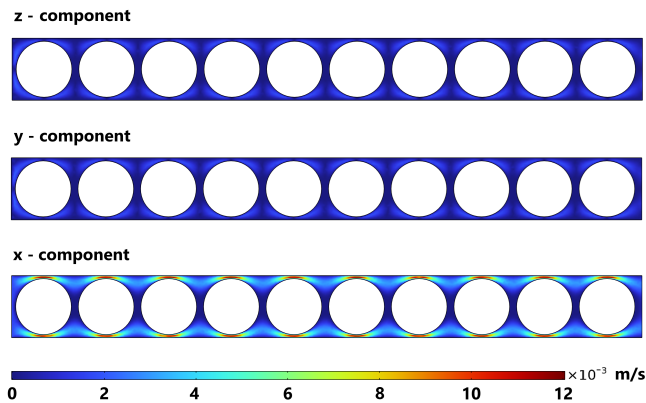


Figure 6: Velocity field along a longitudinal plane for the case $N = 10$.

In Figure 6 we present the velocity field for the case $N = 10$ along a longitudinal plane. The magnitudes of the z and y components of the velocity field are very small when compared to the magnitudes of the x component. Focusing on the x component, we observe that the velocity is much larger on the regions where the spheres are closer to the column wall. This behaviour has two origins. First, it arises in regions with smaller cross-sections, which necessitate faster flow to maintain mass conservation under the incompressibility condition. Second, the flow pattern around each sphere exhibits the characteristic behavior of flow over a sphere [25]: low velocities at the front and rear, and high velocities along the sides.

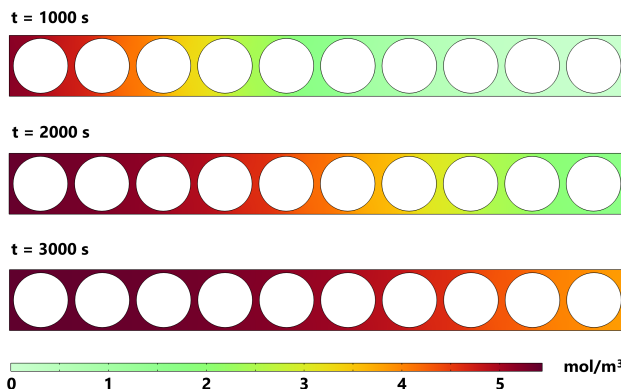


Figure 7: Concentration color maps for the case $N = 10$ at times $t = 1000$ s, 2000 s, 3000 s.

In Figure 7 we present the evolution of the concentration of CO_2 within the column for the case $N = 10$. The progression of CO_2 reassembles that of a planar front wave propagating from left to right. This traveling wave behavior, is a characteristic feature of column adsorption problems which has been extensively studied in 1D models by the authors and collaborators (see, for instance, [10, 12]).

Since any 1D approximation to the problem involves some degree of averaging over a cross section of the column, an important aspect to analyse from the 3D computational experiments is the radial distribution of contaminant. By looking at Figure 7, we observe that the primary variation in contaminant distribution occurs along the axial direction, while the radial direction exhibits a uniform contaminant distribution. To further analyse the radial distribution of contaminant, in Figure 8 we show the evolution of the concentration on a line perpendicular to the x axis that crosses the column between particles number 5 and 6 (i.e., at the center of the column). Panel A clearly shows that the evolution of the concentration is an almost flat profile that increases in time. We note that the configuration for $N = 10$ is radially symmetric, so the evolution on this line is representative of the behaviour on the cross section. A zoom in of the profile at $t = 1400$ s is shown on panel B, indicating a tiny difference of approximately $2.29 - 2.26 = 0.03$ mol/m³ in the concentration between the center and the wall of the column. The minimal variation in concentration across the column's cross sections observed in the 3D experiments validates the use of averaged 1D models under the assumptions of the current study specifically, laminar incompressible Stokes flow and the dilute species approximation.

The general features of flow velocity and concentration observed for the case $N = 10$ persist in the cases $N = 75, 112, 155$, so we skip the discussion of these cases. The equivalent velocity and concentration plots for $N = 75, 112, 155$ are shown in the Supplementary Information.

In the next section, we analyse the differences between the prediction of the 1D and 3D models, focusing on the concentration profiles within the column and the evolution of the concentration at the column outlet.

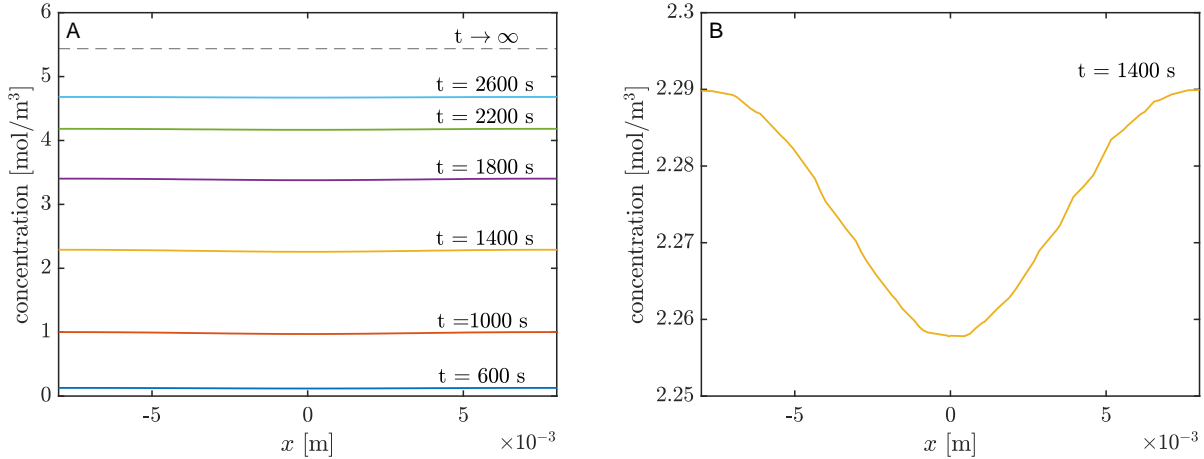


Figure 8: Panel A shows the concentration profiles at the centre of the column for the case $N = 10$ at different times. These correspond to profiles along the line of length $2R$ that goes from $(x, y, z) = (L/2, R, 0)$ to $(x, y, z) = (L/2, -R, 0)$. The dashed line indicates the inlet concentration. Panel B is a zoom of the concentration profile at $t = 1400$ s.

4.3 Assessment of the one-dimensional model

One of the most important measurements used in column adsorption experiments is the concentration of contaminant at the outlet of the column [4]. The time evolution of the concentration at the outlet is named the breakthrough curve. Fitting the solution of a 1D theoretical model to the experimental breakthrough curve is the main procedure by which the adsorption/desorption constants for a particular column experiment are found (see, e.g., [12], [22]). Therefore, testing the limits and assessing the validity of 1D models is critical for accurately predicting the controlling parameters in column adsorption experiments.

In this section, we compare breakthrough curves and concentration profiles obtained from the 1D model and the 3D computational experiments. It is important to note that the microstructure assumed in the homogenization procedure differs significantly from that used in the computational experiments. While both approaches model the adsorbent material using spherical particles, the homogenization framework assumes a periodic array of spheres with diameters much smaller than the adsorption length. In contrast, the computational experiments employ spheres that do not follow the same periodicity and are considerably larger. Rather than attempting to compare two approaches designed to solve the exact same problem, our goal is to demonstrate that, even when the porous medium consists of relatively coarse structures, the 1D model—based on a fine periodic structure—can still provide remarkably accurate predictions of the process.

The dimensionless parameters of the 1D model (27) are found using the parameters and experimental conditions in Table 2: $Da = 1.1 \cdot 10^{-3}$, $Pe^{-1} = 14.34$ and $\delta = 16.78$. Solving

the cell problem (18) numerically with COMSOL and computing the integrals involved in (23) we obtain $\text{Pe}_{\text{eff}}^{-1} = 11$. The solution of the 1D model is obtained numerically implementing a standard forward time and centered in space finite difference scheme in a home-made Matlab code. The authors have used this implementation, or slight variations of it, in several previous works on contaminant capture (see [10, 11, 22], to name a few). Given that the numerical scheme is well-established and poses no significant challenges, we omit a detailed description.

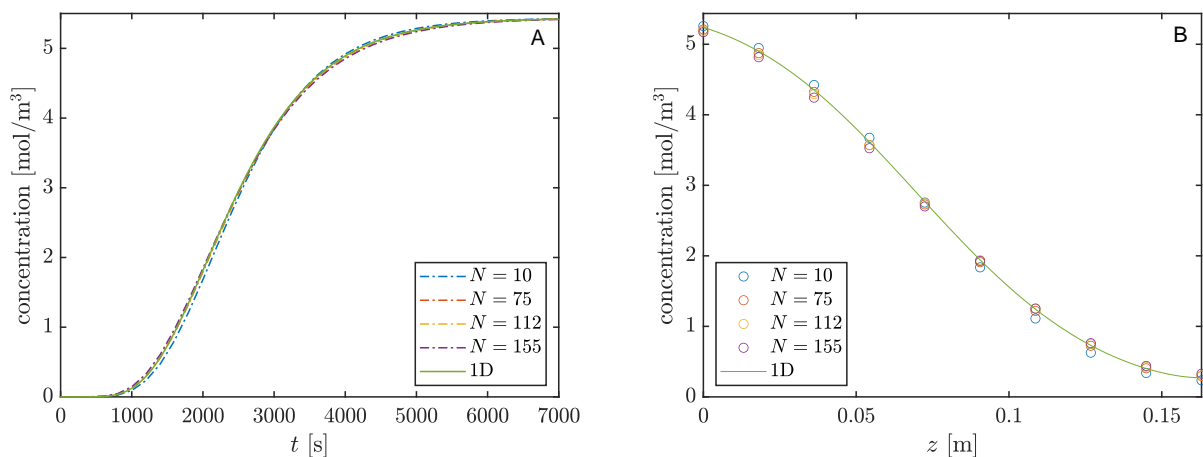


Figure 9: Panel A shows the breakthrough curves for the 3D simulations and the 1D model. The breakthrough curves for the simulations are obtained by averaging over the outlet cross section. Panel B shows the concentration profiles along the z axis at $t = 1400$ s for the 3D simulations and the 1D model. The profiles from the 3D simulations correspond to column cross section averages at 10 equispaced points in the x axis, i.e. $x = pL/9$ for $p = 0, \dots, 9$.

Panel A of Figure 9 presents the breakthrough curves obtained from the 3D computational experiments conducted in this study along with the breakthrough curve from the 1D model. The breakthrough curves from the computational experiments are obtained by averaging the concentration over the outlet cross section. The breakthrough curves for all experiments exhibit remarkable similarity, indicating that the geometry’s microstructure has minimal impact on the overall adsorption process. Moreover, the breakthrough prediction from the 1D model closely matches those from the computational experiments, with the case $N = 10$ showing a slightly greater divergence than the others.

Panel B of Figure 9 compares the concentration profile predicted by the 1D model with the results of the computational experiments along the column at $t = 1400$ s. The circles correspond to cross section averages of the concentration for the four computational cases studied at 10 equispaced yz -planes within the column. The solid line represents the prediction of the 1D model. Once again, the 1D solution effectively captures the trend of the computational experiments, showing a slightly less precise match with the case $N = 10$ compared to the rest.

We now analyse the evolution of the amount of contaminant adsorbed within the column throughout the process. In Figure 10, we show the evolution of the average of the adsorbed fraction over the particle’s surface, $\langle q(t) \rangle = |\partial\Omega_s|^{-1} \int_{\partial\Omega} q(t, \mathbf{x}) dS$. In the case of the 1D model, the average reduces to $\langle q(t) \rangle = L^{-1} \int_0^L q(t, x) dx$. Similar to the concentration profiles and the breakthrough curves, the differences between the four computational experiments and

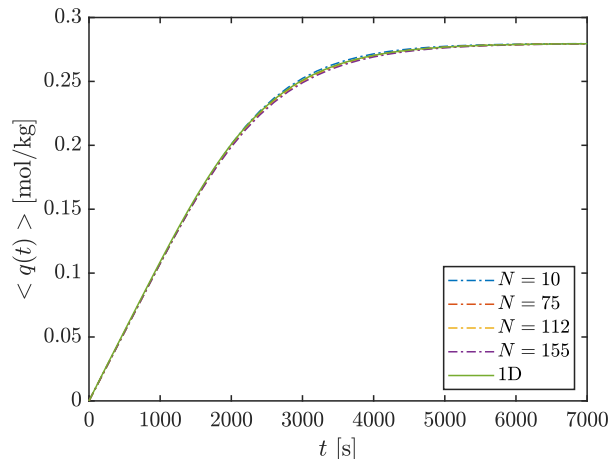


Figure 10: Evolution of the averaged adsorbed fraction over the particle’s surface for each case ($N = 10, 75, 112, 155$) and comparison to the averaged adsorbed fraction from the 1D model.

the 1D model are tiny. Confirming that the microstructure of the media has a tiny impact on the overall adsorption process.

5 Conclusions

In this work, we have investigated the process of contaminant capture via column adsorption, which is one of the most viable methods to actively remove greenhouse gases from the atmosphere to combat global warming. We have formulated a 3D mathematical model that consists of an advection-diffusion equation for the contaminant transport, an equation describing the fluid motion for laminar incompressible flows, and an equation describing the adsorption dynamics of the contaminant on the walls of the porous media. A novelty of our approach is the description of adsorption through an equation defined on the surface of the porous medium, which is coupled to the advection-diffusion equation for the contaminant transport. In contrast, previous 3D models typically represented adsorption using simplified or effective boundary conditions for the advection-diffusion equation.

We performed computational experiments involving the numerical solution of the 3D model on idealised microstructure configurations formed by spherical packings. Increasing the number of particles in each experiment, and adjusting the particles radius to keep the porosity constant, allowed to specifically investigate the effect of microstructure changes in the contaminant capture process. The analysis of concentration profiles and breakthrough curves of the different experiments showed that the microstructure configuration has minimal impact on the process, as the results are nearly indistinguishable. Of course, this conclusion is restricted to the level of approximations used in the current study, i.e. transport of laminar incompressible diluted mixtures in idealised porous media structures.

Assuming a porous media formed by a periodic array of spheres and applying the method of multiple-scale homogenization, we rigorously derived an averaged 3D model of the process, which we then reduced to 1D. The resulting 1D model has the equivalent mathematical form than other 1D models used to describe column adsorption in the literature. However, our

rigorous derivation yields a dispersion coefficient that explicitly incorporates microstructural details, whereas other models rely on experimental correlations or fitting procedures.

In order to assess the capacity of the 1D model to describe the column adsorption process, we solved the 1D model numerically and compared the resulting breakthrough curves and concentration profiles with those from the computational experiments. We found that the solution of the 1D model is extremely close to the results of the computational experiments, showing a slightly greater divergence with the experiment containing the smallest number of particles ($N = 10$). These results confirm that 1D models can accurately describe column adsorption experiments, with minimal influence from the porous media microstructure, as long as the contaminant is sufficiently diluted in the mixture and flow rates in the column are slow.

Supplementary information

In Figures 11–13, we present the velocity fields for the cases with $N = 75, 112, 155$. On each figure, the top panel corresponds to the z -component of the velocity on the zx -plane, while the y and x velocity components are visualized on the xy -plane. Overall, the velocity fields indicate that the x -component reaches maximum values around one order of magnitude larger than in the y and z -components.

In Figures 14–16, we present the evolution of the concentration of contaminant within the column for the cases $N = 75, 112, 155$. The way in which the contaminant propagates through the column is the same than in the $N = 10$ case described in the main text, indicating a little contribution of the microstructure of the porous media on the concentration distribution of contaminant.

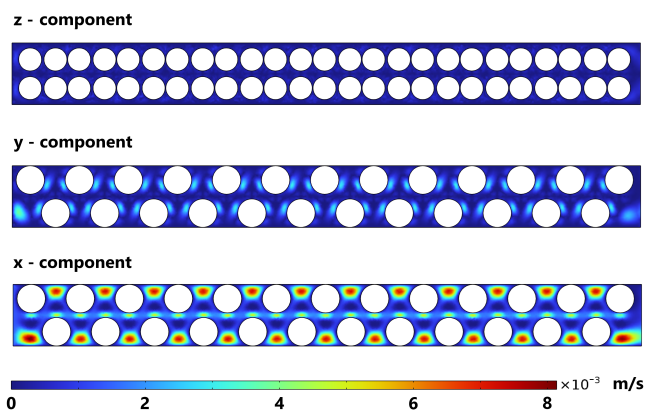


Figure 11: Velocity field along a longitudinal plane for the case $N = 75$.

Author contributions

MA, FF: Conceptualization, Methodology, Investigation, Formal analysis, Writing – original draft, Writing – review & editing.

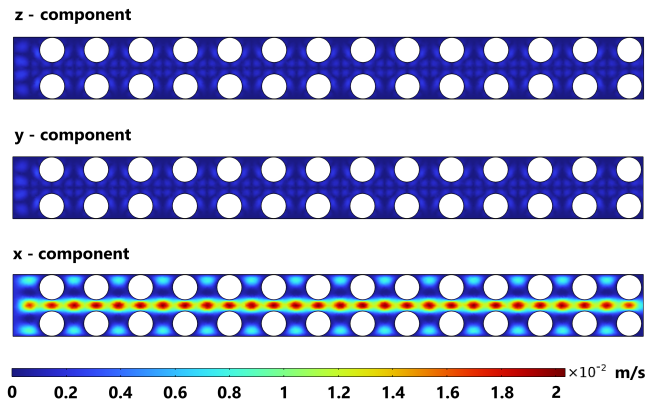


Figure 12: Velocity field along a longitudinal plane for the case $N = 112$.

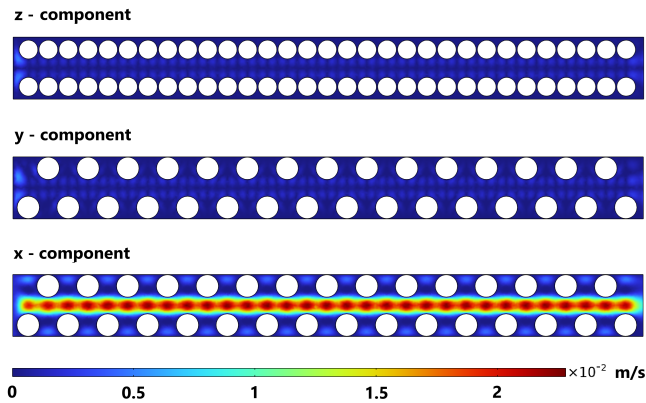


Figure 13: Velocity field along a longitudinal plane for the case $N = 155$.

Acknowledgments

This work is funded by the research project TED2021-131455A-I00 of the Agencia Estatal de Investigación (Spain). M. Agualeles acknowledges the support of the “consolidated research group” (Ref. 2021-SGR-01352) of the Catalan Ministry of Research and Universities. F. Font gratefully acknowledges the SRG programme (Ref. 2021-SGR-01045) and the Serra-Hunter Programme of the Generalitat de Catalunya.

Conflict of interest

All authors declare no conflicts of interest in this paper.

References

- [1] [10.1007/s10311-023-01589-z] M. Karimi, M. Shirzad, J.A.C. Silva, A.E. Rodrigues, Carbon dioxide separation and capture by adsorption: a review, *Environ. Chem. Lett.*, **21** (2023), 2041–2084.

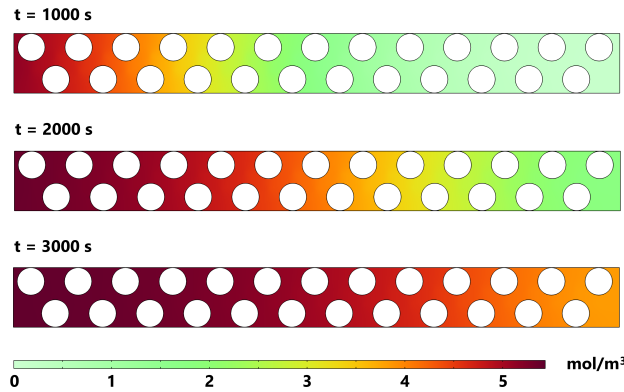


Figure 14: Concentration color maps for the case $N = 75$ at times $t = 1000$ s, 2000 s, 3000 s.

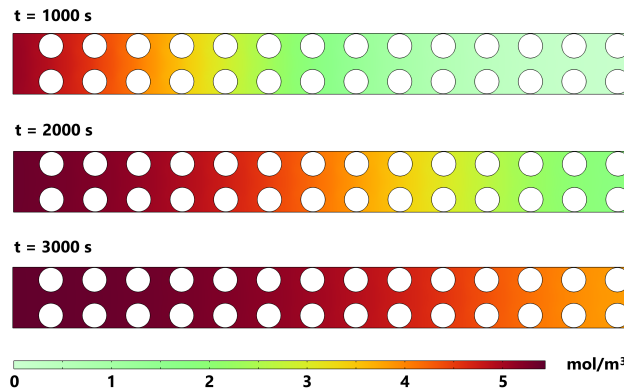


Figure 15: Concentration color maps for the case $N = 112$ at times $t = 1000$ s, 2000 s, 3000 s.

- [2] [10.1016/j.jece.2021.106347] T. Hong, L. Wei, K. Cui, Y. Dong, R. Li, T. Zhang, Y. Zhao, L. Luo, Adsorption performance of volatile organic compounds on activated carbon fibers in a fixed bed column, *J. Environ. Chem. Eng.*, **9** (6) (2021), 106347,
- [3] [10.1016/j.ecoenv.2017.12.012.] M.J. Ahmed, B.H. Hameed, Removal of emerging pharmaceutical contaminants by adsorption in a fixed-bed column: A review, *Ecotoxicol. Environ. Saf.*, **149** (2018), 257-266.
- [4] A. Gabelman, *Adsorption basics: Part 1*, Chemical Engineering Progress **113** (7) (2017), 48–53.
- [5] [10.1007/s13201-019-0927-7] H. Patel, Fixed-bed column adsorption study: a comprehensive review, *Appl. Water Sci.*, **9** (2019), 45.
- [6] [10.1007/s13399-024-05605-2] P.K. Meena, A. Pal, A comprehensive review on methane enrichment in biogas through the purification process using biomass-based adsorbents, *Biomass Conv. Bioref.*, (2024).
- [7] [10.1016/0167-7799(94)90046-9] H.A. Chase, Purification of proteins by adsorption chromatography in expanded beds, *Trends in Biotechnology*, **12**(8) (1994), 296-303.

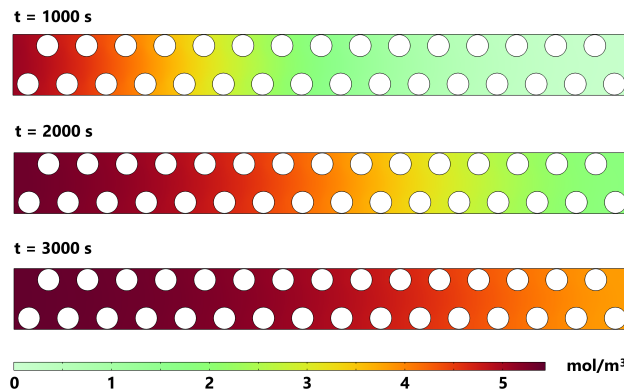


Figure 16: Concentration color maps for the case $N = 155$ at times $t = 1000$ s, 2000 s, 3000 s.

- [8] [10.1016/j.ijheatmasstransfer.2022.123660] T. G. Myers, A. Cabrera-Codony, A. Valverde, On the development of a consistent mathematical model for adsorption in a packed column (and why standard models fail), *Int. J. Heat Mass Transf.*, **202** (2023), 123660.
- [9] [10.1016/j.ces.2019.115205] R. Mondal, S. Mondal, K. V. Kurada, S. Bhattacharjee, S. Sengupta, M. Mondal, S. Karmakar, S. De, I. M. Griffiths, Modelling the transport and adsorption dynamics of arsenic in a soil bed filter, *Chem. Eng. Sci.* **210** (2019) 115205.
- [10] [10.1016/j.apenergy.2020.115565] T. Myers, F. Font, M. Hennessy, Mathematical modelling of carbon capture in a packed column by adsorption, *Appl. Energy*, **278** (2020), 115565.
- [11] [10.1016/j.ijheatmasstransfer.2020.120374] T. Myers, F. Font, Mass transfer from a fluid flowing through a porous media, *Int. J. Heat Mass Transf.*, **163** (2029), 120374.
- [12] [j.physd.2023.133690] M. Agualeles, E. Barrabés, T. Myers, A. Valverde, Mathematical analysis of a sips-based model for column adsorption, *Phys. D*, **448** (2023), 133690.
- [13] [10.1016/j.apm.2024.03.023] L. C. Auton, M. Agualeles, A. Valverde, T. G. Myers, M. Calvo-Schwarzwalder, An analytical investigation into solute transport and sorption via intra-particle diffusion in the dual-porosity limit, *Appl. Mathemat. Modell.*, **130** (2024), 827–851.
- [14] [j.ijheatmasstransfer.2023.124724] A. Valverde, A. Cabrera-Codony, M. Calvo-Schwarzwalder, T. G. Myers, Investigating the impact of adsorbent particle size on column adsorption kinetics through a mathematical model, *Int. J. Heat Mass Transf.*, **218** (2024), 124724.
- [15] [10.1098/rspa.2015.0464], M.P. Dalwadi, I.M. Griffiths, M. Bruna, Understanding how porosity gradients can make a better filter using homogenization theory, *Proc. R. Soc. A: Math. Phys. Eng. Sci.*, **471** (2015), 20150464.

- [16] [10.1016/j.seppur.2005.08.011] J. A. Delgado, M. A. Uguina, J. L. Sotelo, B. Ruiz, Fixed-bed adsorption of carbon dioxide–helium, nitrogen–helium and carbon dioxide–nitrogen mixtures onto silicalite pellets, *Sep. Purif. Technol.*, **49** (1) (2006), 91–100.
- [17] [10.1021/acs.energyfuels.5b00653] M.S. Shafeeyan, W.M.A.. Wan Daud, A. Shamiri, N. Aghamohammadi, Modeling of Carbon Dioxide Adsorption onto Ammonia-Modified Activated Carbon: Kinetic Analysis and Breakthrough Behavior, *Energy & Fuels*, **29** (10) (2015), 6565-6577.
- [18] [10.1016/j.micromeso.2022.111818] L.F.A.S. Zafanelli, A. Henrique, H. Steldinger, J.L. Diaz de Tuesta, J. Gläsel, A.E. Rodrigues, H.T. Gomes, B.J.M. Etzold, J.A.C. Silva, 3D-printed activated carbon for post-combustion CO₂ capture, *Micropor. Mesopor. Mat.*, **335** (2022), 111818.
- [19] [10.1016/j.apenergy.2019.01.042] Q. Chen, F. Rosner, A. Rao, S. Samuelsen, A. Jayaraman, G. Alptekin, Simulation of elevated temperature solid sorbent CO₂ capture for pre-combustion applications using computational fluid dynamics, *Applied Energy*, **237** (2019), 314-325.
- [20] [10.1016/0009-2509(53)80001-1] P. Danckwerts, Continuous flow systems: Distribution of residence times, *Chem. Eng. Sci.*, **2** (1) (1953), 1–13.
- [21] [10.1016/0009-2509(59)80063-4] J. Pearson, A note on the “Danckwerts” boundary conditions for continuous flow reactors, *Chem. Eng. Sci.*, **10** (1959), 281–284.
- [22] [10.1016/j.icheatmasstransfer.2025.108652] T. G. Myers, M. Calvo-Schwarzwalder, F. Font, A. Valverde, Modelling large mass removal in adsorption columns, *Int. Commun. Heat Mass Transf.*, **163** (2025), 108652.
- [23] D. S. Dandy, Bioanalytical microfluidics program, transport property evaluation, <https://navier.engr.colostate.edu/code/code-2/index.html> [Accessed: 30/10/2024] (2024).
- [24] [10.1103/PhysRevE.85.051305] A. Mughal, H. K. Chan, D. Weaire, S. Hutzler, Dense packings of spheres in cylinders: Simulations, *Phys. Rev. E*, **85** (2012), 051305.
- [25] F. P. Incropera, D. P. Dewitt, T. L. Bergman, A. S. Lavine, *Fundamentals of heat and mass transfer*, John Wiley & Sons, Hoboken, NJ, 2017.